

Activatable Hybrid Polyphosphazene-AuNP Nanoprobe for ROS Detection by Bimodal PA/CT Imaging

Mathilde Bouché,[†] Manuel Pühringer,[§] Aitziber Iturmendi,[§] Ahmad Amirshaghghi,[‡] Andrew Tsourkas,[‡] Ian Teasdale,[§] and David P. Cormode^{*,†,‡,§}

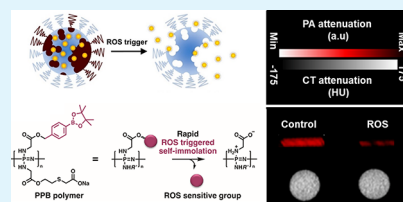
[†]Department of Radiology and [‡]Department of Bioengineering, School of Engineering and Applied Sciences, University of Pennsylvania, Philadelphia, Pennsylvania 19104, United States

[§]Institute of Polymer Chemistry, Johannes Kepler University Linz, Altenberger Straße 69, 4040 Linz, Austria

Supporting Information

ABSTRACT: Overproduction of reactive oxygen species (ROS) is often related to inflammation or cancer and can cause tissue damage. Probes that have been previously reported to image ROS typically rely on imaging techniques that have low depth penetration in tissue, thus limiting their use to superficial disease sites. We report herein a novel formulation of hybrid nanogels loaded with gold nanoparticles (AuNP) to produce contrast for computed tomography (CT) and photoacoustics (PA), both being deep-tissue imaging techniques. The polyphosphazene polymer has been designed to selectively degrade upon ROS exposure, which triggers a switch-off of the PA signal by AuNP disassembly. This ROS-triggered degradation of the nanoprobes leads to a significant decrease in the PA contrast, thus allowing ratiometric ROS imaging by comparing the PA to CT signal. Furthermore, ROS imaging using these nanoprobes was applied to an in vitro model of inflammation, that is, LPS-stimulated macrophages, where ROS-triggered disassembly of the nanoprobe was confirmed via reduction of the PA signal. In summary, these hybrid nanoprobes are a novel responsive imaging agent that have the potential to image ROS overproduction by comparing PA to CT contrast.

KEYWORDS: gold nanoparticles, polyphosphazene, ROS, photoacoustic, computed tomography



1. INTRODUCTION

Reactive oxygen species (ROS) are ubiquitous signaling molecules in tissues affected by many diseases such as cancer, inflammatory bowel disease, and so forth.^{1,2} In addition, ROS damage can alter the normal function of cells, which eventually evolves into tissue inflammation. Therefore, the detection of ROS is important for the prevention and early diagnosis of diseases.³ Yet, most clinical approaches for the measurement of ROS production involve an ex vivo analysis of human fluids or tissues, which is slow and has issues of reproducibility.⁴ Due to those concerns, much work has focused on the detection of ROS using medical imaging techniques. Despite the developments in this field by electron paramagnetic resonance (EPR), fluorescence, and so forth, several challenges remain to be tackled.^{5,6} The limited image resolution and instrumental limitations that restrict the sensitivity of EPR, and the limited depth penetration of fluorescence are constraints in the development of accessible and reliable ROS imaging. Moreover, the nonbiodegradability of the probes and the synthetic challenges to reach an emission wavelength in the near-infrared window are shortcomings that limit the range of detectable diseases. Consequently, an ideal approach for the detection of endogenous ROS overproduction would be (1) minimally invasive, (2) allow the detection of ROS in deeply located tissues, and (3) would be quantifiable to confirm that the change in imaging contrast relates to the response of the probe to ROS instead of a low probe concentration.

Photoacoustic (PA) imaging is a noninvasive technique that allows real-time and dynamic visualization of pathologic events.^{7–9} PA has high spatial resolution compared to other optical imaging modalities and can provide volumetric information. Moreover, PA has recently received growing attention as an ROS imaging modality using activable probes of various types, namely, activable dyes,¹⁰ biomimetic material,^{11,12} or nanoparticles.^{13–17} For the detection and follow-up of probe excretion, computed tomography (CT) is a powerful technique that produces images of high spatial and temporal resolution while being commonly available. Moreover, attenuation in CT is linearly correlated to the AuNP concentration, which allows probe quantification. Therefore, the development of a ROS-sensitive probe that provides contrast in both PA and CT is highly appealing for imaging of diseased sites overexpressing ROS and inflammatory responses.

Spherical AuNP have a localized surface plasmon resonance (LSPR), which is responsible for their high absorbance band between 500 and 600 nm (with the wavelength increasing as their size increases). Close proximity of AuNP causes a collective plasmon resonance that translates into a strong bathochromic shift of absorbance into the near-infrared region (NIR).^{18–20} This difference in optical properties

Received: May 17, 2019

Accepted: July 19, 2019

Published: July 19, 2019



between single AuNP and their engineering into assembled nanostructures has elicited strong interest, especially for applications as biosensors,²¹ phototherapy,^{22,23} or biomedical imaging.^{24,25} In this area, we have recently reported hybrid nanogels where the assembly of a AuNP payload in a polyphosphazene core provides strong contrast enhancement in CT imaging as well as PA owing to the dense packing of AuNP.²⁶ Moreover, polyphosphazene functionalization with an arylboronate moiety efficiently allows its H₂O₂-triggered degradation into low molecular weight byproducts.²⁷ Therefore, we sought to combine these technologies to develop a hybrid nanoprobe that would display both CT and PA contrasts and selectively disassemble under an ROS trigger to provide a loss of PA contrast while maintaining its CT contrast (Figure 1). This strategy relies on the detection of ROS by

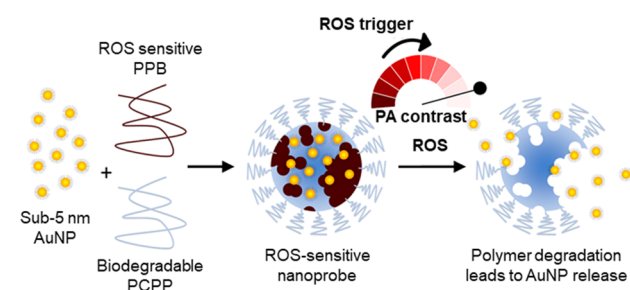
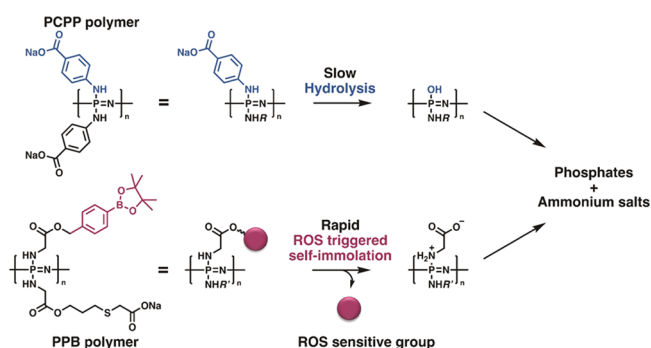


Figure 1. Assembly of AuNP in nanogels that selectively degrade under ROS exposure and release free AuNP for imaging of ROS with PA.

comparing the decreased contrast in PA to the constant CT contrast and has a potential for the detection of deeply lying ROS. Moreover, the use of bimodal imaging is effective for probe quantification, thus ensuring reliable ROS detection. Toward this aim, small excretable gold nanoparticles (sub-5 nm AuNPs) that are biocompatible, photostable, and provide strong CT contrast enhancement are assembled into polymeric nanogels composed of polyphosphazenes to provide PA contrast thanks to the collective plasmon coupling.²⁸ The nanogels are composed of two polyphosphazene derivatives: poly[di(carboxylatophenoxy)phosphazene] (PCPP) and the arylboronate polyphosphazene derivative (PPB) (Scheme 1). PCPP is biodegradable and releases nontoxic and neutral pH byproducts.²⁹ Moreover, we have shown the potential of PCPP nanogels as a carrier for AuNP, affording a highly biocompatible CT and PA contrast agent.^{26,30} On the other

Scheme 1. Degradation Pathways of PCPP (Upper) and the ROS-Sensitive PPB (Lower) Yielding Neutral pH and Nontoxic Byproducts



hand, PPB is designed to selectively degrade when exposed to ROS to achieve a ROS-triggered disassembly and release the AuNP payload, hence changing the PA signal. This nanoprobe combining a biodegradable polyphosphazene that hydrolyzes to ammonium and phosphate, with sub-5 nm AuNP that are excretable through the kidneys, was designed to be fully degradable in biological environments and be swiftly excreted through urine or feces to avoid long term retention. We report herein a hybrid nanoprobe, referred to as PPB NP in this manuscript, has high biocompatibility in vitro, efficiently disassembles, and displays a PA signal switch-off in response to ROS exposure both in solution and in macrophages, thus allowing endogenous ROS imaging by comparing the PA to CT contrast.

2. EXPERIMENTAL SECTION

Gold(III) chloride trihydrate, sodium borohydride, poly-di-(carboxylatophenoxy)phosphazene disodium salt (PCPP, 1 MDa), spermine, reduced L-glutathione, hydrogen peroxide (H₂O₂), ferrous perchlorate hydrate (Fe(ClO₄)₂·xH₂O), potassium dioxido (KO₂), and lipopolysaccharides (LPS) were purchased from Sigma-Aldrich (St. Louis, MO). PEG-PLL (PEG M_w 5000/PLL M_w 4900) was purchased from Alamanda Polymers. Recombinant human interferon-γ protein (IFN-γ) was purchased from Abcam. For the microfluidic setup, the herringbone mixer microfluidic chip (channel diameter of 600 μm) and male luers were purchased from Microfluidic ChipShop (Jena, Germany), the polyethylene tubing from VWR (Philadelphia, PA), and the syringe pumps from Braintree Scientific (Braintree, MA). HepG2, RAW264.7, Renca, and SVEC4-10 cell lines were purchased from ATCC (Manassas, VA). LIVE/DEAD assay kits were purchased from Invitrogen (Grand Island, NY). Cells were cultured in Dubecco's Modified Eagle Medium from Invitrogen (Grand Island, NY) supplemented with 1% penicillin and 10% fetal bovine serum unless specified otherwise. TNF-α ELISA kit was purchased from Invitrogen (Grand Island, NY).

The experimental details for the synthesis of the arylboronate polyphosphazene derivative (PPB) are detailed in the [Supporting Information](#).

2.1. Nanoparticle Syntheses. The glutathione-coated AuNP and PCPP NP were produced according to our previously reported procedure.²⁶ By adaptation of a procedure previously reported by us,²⁶ the PPB NPs were obtained by injection in a herringbone microfluidic chip at a flow rate of 6 mL·min⁻¹ of a solution of PPB (1.5 mg in DPBS at 1 mg·mL⁻¹), PCPP (0.5 mg, in DPBS at 1 mg·mL⁻¹), and AuNP (5 mg) in parallel to spermine (1.96 mg in DPBS at 0.98 mg·mL⁻¹, pH 7.4) and PEG-PLL (0.17 μg in DPBS at 0.085 μg·mL⁻¹). The mixture collected from the microfluidic chip was then poured in a CaCl₂ solution (100 mL, in DI H₂O at 88 g·mL⁻¹) and allowed to stir for 20 min. NPs were further purified by centrifugation (2k rpm, 8 min) and washing with DI H₂O three times. Finally, the NP suspension was concentrated and stored at 4 °C in DI H₂O.

2.2. Characterization Methods. ¹H NMR spectroscopy was recorded on a Bruker 300 MHz spectrometer using the residual solvent peak as a reference. ³¹P NMR (121 MHz) measurements were performed using 85% phosphoric acid as an external standard. Gel permeation chromatography (GPC) measurement was carried out on a Viscotek HT-GPC instrument equipped with three GRAM columns (combination medium, 300 × 8 mm, 10 μm particle size) from PSS (Germany). DMAc with 57.6 mM LiBr and 0.1 M acetic acid was used as an eluent at a flow rate of 0.75 mL·min⁻¹ at 70 °C. Multidetector calibration (refractive index detector, viscometer and light scattering detector) was used to estimate the molecular weight of the polymer.

The nanoparticles were characterized by UV–visible spectroscopy on a UV–visible spectrophotometer (Thermo Fisher Scientific, USA) after dilution in DI water, transmission electron microscopy acquired at 80 keV using a JEOL 1010 microscope (JEOL, Tokyo, Japan) with an AMT NanoSprint500 5 Megapixel camera (AMT, Woburn, MA),

USA), scanning electron microscopy, and energy-dispersive X-ray spectroscopy elemental mapping performed on a JEOL 7500F microscope operated at 15 kV (JEOL, Tokyo, Japan) with an EDAX Octane Elect EDS detector (Mahwah, NJ, USA), and Fourier transform infrared (FT-IR) spectroscopy by grinding 5 μL of sample with 100 mg KBr, pressing into pellets, and analyzed on a JASCO FT/IR-480 PLUS. The elemental gold concentrations were determined by inductively coupled plasma optical emission spectroscopy (ICP-OES) on 10 μL samples digested in 1 mL of aqua regia and diluted to a final volume of 6 mL with DI H_2O .

2.3. Evaluation of ROS Sensitivity. The NPs were prepared in microcentrifuge tubes at a gold concentration of 0.5 $\text{mg}\cdot\text{mL}^{-1}$ and a volume of 1 mL DI H_2O supplemented with several ROS species (i.e., H_2O_2 or ClO^- or O_2^- or OH^\cdot) and incubated in a water bath at 37 $^\circ\text{C}$. At the desired time points, samples were vortexed, centrifuged at 2k rpm for 8 min, and the supernate was collected for quantification of the released cargo by ICP-OES. One milliliter of a freshly prepared incubation medium was rapidly added to each sample, and all were vortexed and allowed to incubate at 37 $^\circ\text{C}$ until the next time point. H_2O_2 was diluted from commercially available solutions. Both ClO^- and O_2^- were generated by dilution of commercially available solutions of NaOCl and KO_2 , respectively. OH^\cdot was generated in situ by reaction of $\text{H}_2\text{O}_2/\text{Fe}(\text{ClO}_4)_2$ in a 10:1 molar ratio.

2.4. Computed Tomography and Photoacoustic Instrumentation. Computed tomography (CT) imaging was performed on nanoparticles at gold concentrations ranging from 0 to 5 $\text{mg}\cdot\text{mL}^{-1}$, suspended in agar gel (1% in DI H_2O) in 250 μL vial tubes and secured in a plastic rack. Each sample was prepared in triplicate. CT images were acquired using a MiLabs $\mu\text{-CT}$ and operated at a tube voltage of 55 kV and tube current of 190 μA with a 75 ms exposure. The image reconstruction was performed with a slice thickness of 100 μm and a 0.1 mm increment. OsiriX (v.3.7.1 64-bit software) was used to analyze the images. ROI values were recorded on five slices for a circular area drawn on the coronal view of each tube. The ROI values were normalized to the NP-free agarose gel. The reported attenuation value for each concentration corresponds to the average of triplicate samples of the selected concentration.

Photoacoustic (PA) imaging was done on NPs in solution, at gold concentrations ranging from 0 to 1 $\text{mg}\cdot\text{mL}^{-1}$, loaded into PE tubes (inner diameter 0.5 mm), and mounted into a plastic holder immersed in DI H_2O . The PA signals were acquired at an excitation wavelength of 700 nm, a PA gain, 40 dB; priority, 95%, and a distance of 10 mm from the transducer in 3D mode. The LZ550 transducer was utilized (axial resolution, 44 μm ; broadband frequency, 32–55 MHz). The images were analyzed using ImageJ (v.1.51 k software). The ROI values were recorded for a circular area drawn on the section of each tube and averaged. The ROI values were normalized in respect to DI water.

2.5. In Vitro Biocompatibility. HepG2, Renca, SVEC4-10, and RAW264.7 cell lines were cultured according to the supplier instructions, and their cell viability after incubation with PPB NP was assessed using the LIVE/DEAD assay. Experiments were performed in triplicate. Cells were plated in 35 mm dishes with 20 mm bottom wells at a cell density of 100 k cells per well. After 24 h, cells were treated with PPB NPs at concentrations of 0, 0.125, 0.25, and 0.5 $\text{mg}\cdot\text{mL}^{-1}$. After 8 h of incubation at 37 $^\circ\text{C}$ in a 5% CO_2 atmosphere, the cells were washed with DBPS twice and incubated for 20 min with 400 μL of LIVE/DEAD cocktail (0.1% stock athidium-1 homodimer and 0.025% stock aalcein AM in DPBS). Three images of four different areas of the well were acquired using two excitation/emission filter pairs: 495–515 nm for live cells dye and 528–617 nm for dead cells dye. A custom MATLAB code was used to count the number of cells for each filter pair in each image, and the ratio of dead cells to living cells was calculated as the viability measurement.

2.6. Endogenous ROS Quantification by Carboxy- H_2DCFDA Assay. First, RAW264.7 macrophages were cultured in 96-well plates at a density of 10^5 cells per well for 18 h. The cells were then washed gently with DPBS, treated with 100 μL of either DPBS or a stimulation cocktail of LPS (1 $\mu\text{g}\cdot\text{mL}^{-1}$) and IFN- γ (50 $\text{ng}\cdot\text{mL}^{-1}$) in DPBS, and incubated for 4 h at 37 $^\circ\text{C}$ in a 5% CO_2 in a humidified

incubator. Thirty minutes before the end of cell stimulation, each well was treated in the dark with 100 μL of a 15 μM solution of carboxy- H_2DCFDA in DPBS. The negative control for cell autofluorescence was cells incubated with DPBS alone, and the positive control was cells incubated with both 100 μL of a 100 mM H_2O_2 solution in DPBS and 100 μL of a 15 μM solution of carboxy- H_2DCFDA in DPBS. Each condition was prepared in triplicate. After 30 min incubation at 37 $^\circ\text{C}$ in a 5% CO_2 in a humidified incubator, the fluorescence results under excitation wavelength of 485 nm and emission at 528 nm were recorded using a plate reader (Synergy H1, BioTek, VT).

2.7. Endogenous TNF- α Expression by ELISA Assay. First, RAW264.7 macrophages were cultured in 96-well plates at a density of 10^5 cells per well for 18 h. The cells were then washed with DPBS, treated with either DMEM cell medium (no FBS) or a stimulation cocktail of LPS (1 $\mu\text{g}\cdot\text{mL}^{-1}$) and IFN- γ (50 $\text{ng}\cdot\text{mL}^{-1}$) in DMEM (no FBS), and incubated for 4 h. The supernate was then collected and used in the ELISA assay according to the kit instructions. The absorbance was measured using a plate reader (Synergy H1, BioTek, VT).

2.8. Preparation of Cells for TEM. The RAW264.7 macrophages were cultured in 6-well plates at a density of 2×10^6 cells per well for 18 h. The cells were then washed with DPBS, treated with either DMEM cell medium (no FBS) or a stimulation cocktail of LPS (1 $\mu\text{g}\cdot\text{mL}^{-1}$) and IFN- γ (50 $\text{ng}\cdot\text{mL}^{-1}$) in DMEM (no FBS), and incubated for 4 h. Each well was treated with the NP suspension at a final gold concentration of 0.1 $\text{mg}\cdot\text{mL}^{-1}$ and incubated for 4 h. The cells were washed twice with DPBS, freed from the plate by scraping in DMEM, and centrifuged (1k rpm, 5 min). Finally, the cell pellets were fixed in a solution of 2.5% glutaraldehyde and 2% formaldehyde, cut into 60 nm-thick sections, stained, and placed onto TEM grids.

2.9. Preparation of Cells for PA and CT Imaging. To prepare the agar phantom for PA, a mixture of agarose in DI H_2O (2 w/v %, 1 g in 50 mL) was heated to 40 $^\circ\text{C}$ in a water bath under vigorous stirring until complete agarose dissolution. A layer (0.5 cm) of agar was poured in a dish used as mold and allowed to cool down for 1 h on a flat surface. Pipet tips were placed upside down, and a second layer (0.5 cm) of agarose (2%) was poured and allowed to cool down for an additional 1 h. Then, the pipet tips were gently removed to free the holes dedicated to samples. In parallel, the RAW264.7 macrophages were cultured in 6-well plates at a density of 2×10^6 cells per well for 18 h. The cells were then washed with DPBS, treated with either a DMEM cell medium (no FBS) or a stimulation cocktail of LPS (1 $\mu\text{g}\cdot\text{mL}^{-1}$) and IFN- γ (50 $\text{ng}\cdot\text{mL}^{-1}$) in DMEM (no FBS) and incubated for 4 h. Each well was treated with the NP suspension at a final gold concentration of 0.1 $\text{mg}\cdot\text{mL}^{-1}$ and incubated for 4 h. The cells were washed twice with DPBS, freed from the plate by scraping in DMEM, and centrifuged (1k rpm, 5 min). Finally, the cell pellets were resuspended into warm agar gel (0.5% in DI H_2O , 40 $^\circ\text{C}$), added to each well of the agar phantom (2% in DI H_2O), covered in a layer of agar gel (2% in DI H_2O , 40 $^\circ\text{C}$), and cooled down for 30 min on ice prior to imaging. This phantom was used within the following hours for PA imaging.

For CT, RAW264.7 macrophages were cultured under similar conditions as described above. The cell pellets were resuspended into a solution of 2.5% glutaraldehyde and 2% formaldehyde and allowed to loosely settle for 24 h prior CT imaging.

2.10. Statistical Analysis. Each experiment was performed in a minimum of three replicates unless stated otherwise. The statistical analysis was performed by one-way ANOVA test on Excel software. The data were considered nonstatistically significant for $p > 0.05$.

3. RESULTS AND DISCUSSION

3.1. Synthesis and Characterization of the Degradable Polyphosphazene. We describe here a nanogel formulation using polyphosphazene derivatives that have good qualities for biomedical applications, that is, high water solubility, biocompatibility, and biodegradability into harmless byproducts for rapid clearance (Scheme 1).^{31,32} The

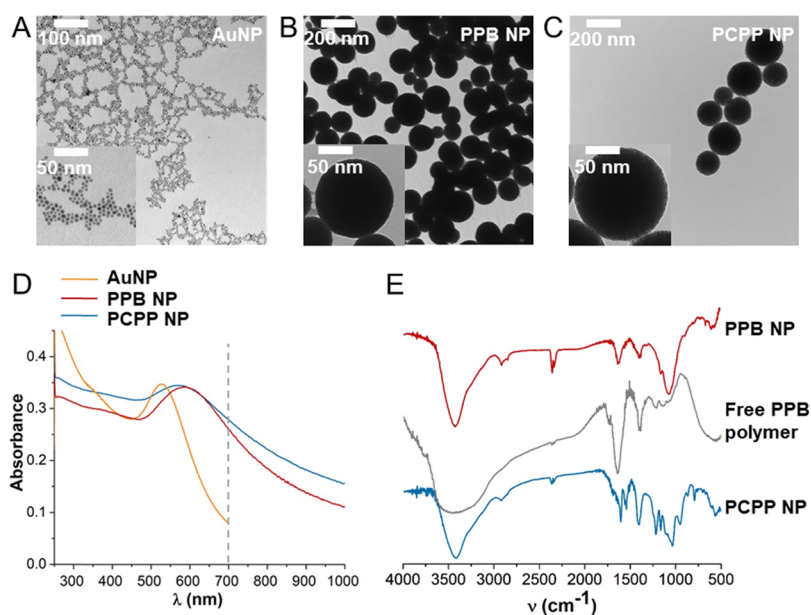


Figure 2. (A)–(C) representative TEM of AuNP (left), PPB NP (center), and PCPP NP (right). (D) UV–visible spectra of the PPB NP (red) compared to the free AuNP (orange) and control PCPP NP (blue); (E) FT-IR spectrum of ROS-sensitive NP (red) compared to the free PPB polymer (grey) and PCPP NP (blue).

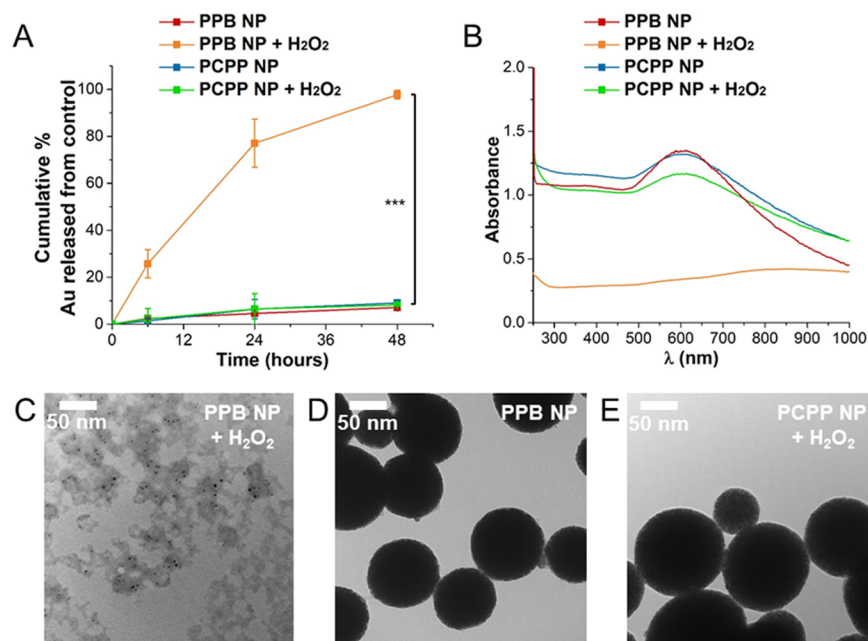


Figure 3. Effects of 10 mM H₂O₂ on the degradation of PPB NP and the control PCPP NP after 48 h. (A) Cumulative gold released determined by ICP-OES. (B) UV–visible spectra. Representative TEM of (C) PPB NP in 10 mM H₂O₂, (D) PPB NP without H₂O₂, and (E) PCPP NP in 10 mM H₂O₂. The symbol *** indicates a statistically significant difference at $p < 0.001$.

arylboronate polyphosphazene PPB is functionalized with a carboxylate substituent, providing aqueous solubility and cross-linking ability by ionic interactions, in addition to a responsive arylboronate substituent (Scheme S1). The arylboronate motif acts as a caging group that readily reacts with ROS to form the unstable glycine-functionalized polyphosphazene, which further undergoes a self-catalyzed backbone degradation into metabolizable phosphates and ammonia (Scheme 1). PPB was readily synthesized in four steps by bulk cationic polymerization of Cl₃PNSiMe₃ to a poly(dichloro)phosphazene, which was further functionalized by a postpolymerization strategy

with glycinate arylboronic acid pinacol ester and allyl glycinate (Scheme S1) to give poly(organo)phosphazenes with a molecular weight (M_w) of approximately 340 000 g·mol⁻¹. Subsequent thiolene addition of thioglycolic acid and deprotonation to the sodium salt gave the final water-soluble polyphosphazene PPB.

3.2. Formulation and Characterization of the ROS-Sensitive Probe. Sub-5 nm gold nanoparticles coated with glutathione (GSH) were synthesized according to a reported method by reduction of gold chloride with sodium borohydride, followed by in situ ligand exchange with the

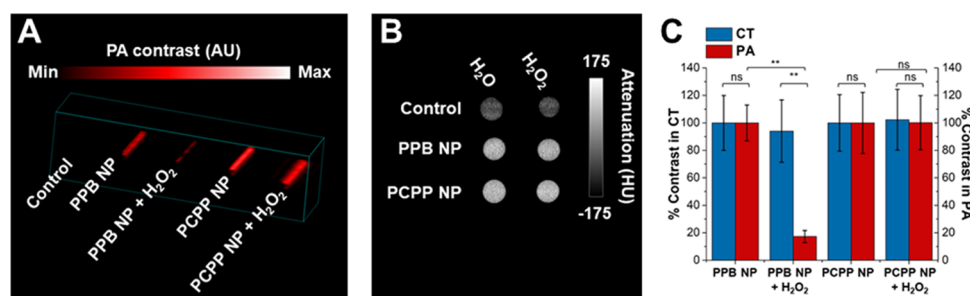


Figure 4. Effect of H₂O₂ incubation for 48 h with PPB and PCPP NPs on their (A) PA contrast and (B) CT contrast. (C) Percentage of contrast enhancement in CT (blue) and PA (red) of the PPB or PCPP NP to control. Experiments done at a gold concentration of 1 mg·mL⁻¹. The symbols ** and 'ns' indicate either a statistically significant difference at $p < 0.01$ or nonstatistically significant differences, respectively. Error bars represent standard deviations after conversion to percentages.

coating agent GSH, and purification by centrifugation (Figure 2A).²⁶ Next, the hybrid nanogels were formulated using a microfluidic device that allows homogeneous mixing of the AuNP and free PPB/PCPP polymers with a spermine cross-linker and forms the AuNP-loaded polymeric nanoparticles in a controlled manner, as previously reported by us.²⁶ This affords spherical PPB nanoparticles (PPB NP) 142.1 ± 38.2 nm in diameter as determined by transmission electron microscopy (TEM; Figure 2B), with a loading efficiency of AuNP of 52%. While the free AuNPs have a maximum absorption peak at a wavelength of 514 nm, their dense assembly into the PPB NP induces a bathochromic shift of their maximum absorption peak to 610 nm resulting from the interparticle plasmon coupling (Figure 2D).²⁸ Of note, this cooperative plasmon coupling phenomenon is responsible for the strong absorption at 700 nm of the PPB NP (dashed line in Figure 2D) compared to dispersed AuNP, thus allowing the use of these PPB NPs as a platform for photoacoustic imaging with laser excitation at 700 nm, close to the NIR region. Moreover, the chemical composition of the polymeric core was confirmed by Fourier transform infrared spectroscopy (FT-IR) owing to the characteristic peaks at $\nu = 1634$ and 1392 cm⁻¹ that can be found both in the spectra of the PPB free polymer and PPB NP (Figure 2E). Additional characterizations by SEM, elemental mapping, and EDX confirmed the morphology and elemental composition of the PPB NP (Figure S1A–D). PCPP NPs loaded with AuNPs, synthesized previously by us, were used as a non-ROS-sensitive control formulation.²⁶ The PCPP NPs are 170.0 ± 49.1 nm in diameter, the AuNP loading efficiency is 68%, and those particles have an intense absorbance at 700 nm (Figure 2C), comparable to the PPB NP. SEM, elemental mapping, and EDX corroborated both the morphology and elemental composition of the PCPP NP (Figure S1E–H).

3.3. Probe Activation by H₂O₂ and Associated Signal in PA and CT. The arylboronate moiety is known to selectively degrade under H₂O₂ exposure, and therefore, the degradability of the PPB NP was investigated by incubations in media containing H₂O₂.²⁷ Both the PPB and control PCPP NPs were incubated with 10 mM H₂O₂, and the amount of AuNP released from the polymeric NP was quantified at selected time points to investigate the degradation profiles of each formulation. The PPB NP released over 97% of their AuNP payload within two days exposure to 10 mM H₂O₂, while the control PPB NP incubated in deionized water released less than 5% of their payload (Figure 3A). Of note, the control PCPP NP incubated both with and without H₂O₂ also

released less than 5% of their total AuNP loading (Figure 3A). Moreover, the disassembly of the PPB NP in H₂O₂ and the release of free AuNP were confirmed by the significant decrease of the absorption intensity at 700 nm observed in UV–vis spectroscopy (Figure 3B). The H₂O₂-triggered degradation of the polymer core of the PPB NP is also visible with TEM as amorphous organic aggregates and released single AuNP that are observed after 48 h exposure to H₂O₂ (Figure 3C). On the contrary, both the PPB NP incubated in water and the PCPP NP in H₂O₂ remained unaffected (Figure 3D,E, respectively). Of note, the PPB NP degraded more quickly upon exposure to both H₂O₂ and O₂⁻ than upon exposure to other ROS species, such as OCl⁻ or OH⁻, which lead to low levels of degradation of the PPB NP (Figure S2).

AuNPs are known to strongly attenuate X-rays and thus provide high CT contrast enhancement with minimal influence from their coating or the distance from their neighboring AuNP. Therefore, we observed that PPB NPs produce strong contrast enhancement that is linearly correlated to the gold concentration (Figure S3A,B), as expected. Moreover, the PPB NPs have strong absorbance at 700 nm due to the interparticle plasmon resonance of AuNP and can be used as contrast agents in photoacoustic imaging. The PPB NP provided a PA signal that linearly correlates to the gold concentration and can be detected at gold concentrations down to 0.125 mg·mL⁻¹ (Figure S3C,D). The PA signal from PPB NP was found to have a maximum intensity at 700 nm and decreases as the excitation wavelength increases (Figure S3E).

We next investigated the influence of the H₂O₂-triggered degradation of PPB NP on their contrast enhancement in both PA and CT. Owing to the low absorbance intensity of a single AuNP compared to the nondegraded PPB NP at 700 nm (Figures 2D and 3B), it is expected that their disassembly would result in a weaker PA signal compared to the nondegraded nanoparticles. The PA signal for PPB NP incubated with 10 mM H₂O₂ was 83% lower than that for PPB NP incubated without H₂O₂ (Figure 4A). On the other hand, the control PCPP NPs that are not sensitive to H₂O₂ and maintain their assembly display an intense PA signal independently of the incubation media (Figure 4A). Of note, the PPB NP degradation was dependent on the H₂O₂ dose, with higher concentrations of H₂O₂ inducing greater release of AuNP (Figure S4A). Moreover, the PA signal showed a signal decrease that correlates with increasing H₂O₂ concentration (Figure S4B).

Since X-ray attenuation depends on the AuNP concentration and not on its immediate surroundings, the CT contrast

enhancement of PPB NP was expected to remain unchanged upon exposure to H_2O_2 . No significant difference in CT contrast enhancement was observed between the PPB NPs incubated with or without H_2O_2 at the same gold concentration (Figure 4B,C). Similarly, the control PCPP NP provided comparable CT contrast enhancement in the two media (Figure 4B,C). Overall, the ROS-sensitive PPB NP provided a significant difference in PA signal intensity depending on the presence of ROS while maintaining a constant CT contrast enhancement. This investigation of the responsiveness in solution of the PPB NP nanoprobe to ROS supports the PA switch-off ability of the PPB NP exposed to H_2O_2 and possible PA to CT contrast comparison to identify ROS overexpression.

3.4. In Vitro Detection of ROS in Macrophages.

Patients suffering pathological conditions such as cancer or inflammatory diseases tend to have local high concentrations of macrophages that overexpress ROS in the tissues affected by inflammation. Therefore, using RAW264.7 macrophages for our study, we investigated the ability of PPB NP to detect endogenous ROS overproduction by PA signal switch off and PA to CT contrast comparison. First, we investigated the viability of four different cell lines: HepG2 (hepatocytes), SVEC4 (endothelial), Renca (kidney), and RAW264.7 (macrophages) after incubation for 8 h with the PPB NP (Figure S5). No significant decrease in the cell viability was observed by LIVE-DEAD assay on all the tested cell lines, thus indicating that the PPB NP formulation was cytocompatible.

To investigate the selective degradability and PA signal switch-off of the PPB NP in inflamed macrophages, RAW264.7 cells were stimulated by 4 h incubation with bacterial cell wall lipopolysaccharide (LPS) and interferon- γ (IFN- γ) according to a previously reported procedure.³³ Elevated ROS levels in stimulated cells were confirmed using a fluorescence assay (Figure S6A). Others have reported such stimulation resulting in elevated ROS throughout the macrophage cells.³³ In addition, the cell inflammatory status was supported by elevated production of TNF- α (Figure S6B). The effects on the nanoparticles taken up by the cells were investigated with TEM. The nonstimulated macrophages efficiently engulfed both PPB and PCPP NPs into endosomes (Figure 5A,B, respectively). However, while the control PCPP NP maintained their spherical shape and dense concentration of AuNP, a marked trend to greater degradation of the ROS-sensitive PPB NP is visible with the loss of shape and release of single AuNP. A similar trend was observed for the stimulated macrophages where the PPB NP became almost completely disassembled (Figure 5C), while the control PCPP NP did not show significant morphological changes (Figure 5D). Therefore, the TEM analysis of the representative macrophages incubated with the nanoparticles suggest ROS-triggered disassembly of the PPB matrix leading to the release of AuNP intracellularly.

Encouraged by these results, we analyzed the PA contrast provided by the stimulated RAW264.7 cells incubated with PPB NP to determine whether a decrease in the PA signal intensity occurs as a consequence of ROS-triggered NP disassembly. While the nonstimulated macrophages that were incubated with the PPB NP have a strong PA signal, a significant decrease of 73% in PA signal is observed in the case of the inflammation-stimulated macrophages (Figure 6A,C). Considering the enhanced disassembly of PPB NP observed with TEM on stimulated cells, the loss of PA signal seems to

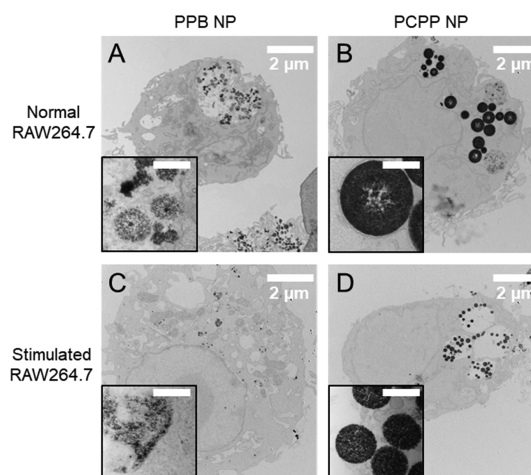


Figure 5. Detection of ROS in a stimulated RAW 264.7 monocyte model of inflammation. Representative TEM images of normal RAW 264.7 cells incubated with (A) PPB NP or (B) PCPP NP, and LPS-stimulated RAW 264.7 monocyte cells after 4 h incubation with (C) the ROS-sensitive NP or (D) the control PCPP NP. The scale bars in the insets corresponds to 200 nm.

arise from the greater ROS production in the inflamed macrophages that triggers the disassembly of the nanoprobe. On the other hand, in the case of the PCPP NPs that are not sensitive to ROS, no significant change in the PA signal is observed between the two macrophages states. Moreover, both stimulated and nonstimulated macrophages incubated with the PPB NP display similar CT attenuation, confirming the possibility to use CT for nanoprobe quantification irrespective of its environment (Figure 6B,C). Similarly, the PCPP NP-treated macrophages display similar contrast enhancement in CT, independently from the cellular ROS level. Overall, we have shown that ROS-responsive switch-off probe PPB NP can differentiate macrophages that overexpress ROS from the noninflamed macrophages by comparing the signal intensity observed in PA and CT.

We found that functionalizing a polyphosphazene backbone with an arylboronate moiety efficiently provided a stimulus-responsive behavior and enhanced ROS-triggered degradation, similarly to other arylboronate polyphosphazene derivatives²⁷ or other functionalized polymers.^{34,35} The PPB polymer we used as a nanogel for the assembly of AuNP was shown to degrade selectively upon ROS exposure within 48 h. Although this proof-of-principle supported our hypothesis, faster ROS-triggered degradation rates have been reported in the case of capsules made of arylboronate functionalized polyester that were capable of selectively releasing 50% of their Nile red payload within 10 h³⁶ or for free dextran functionalized by arylboronate moieties whose half-life was as low as 36 min when exposed to only 1 mM H_2O_2 .³⁷ Accordingly, enhancing the sensitivity of our PPB NP by fine-tuning the polyphosphazene core would be desirable to achieve an improved ROS imaging nanoprobe.

Polyphosphazene-AuNP-based nanoconstructs of differing structures have been reported for nanomedicine use, for example, Chhour et al. reported PCPP-AuNP nanoassemblies where the location of AuNP within the polymeric structure could be controlled and demonstrated their contrast generation in CT.³⁰ Cheheltani et al. highlighted the potential of PCPP-AuNP particles as the biodegradable multimodality contrast agent for use in both CT and PA.²⁶ Interestingly,

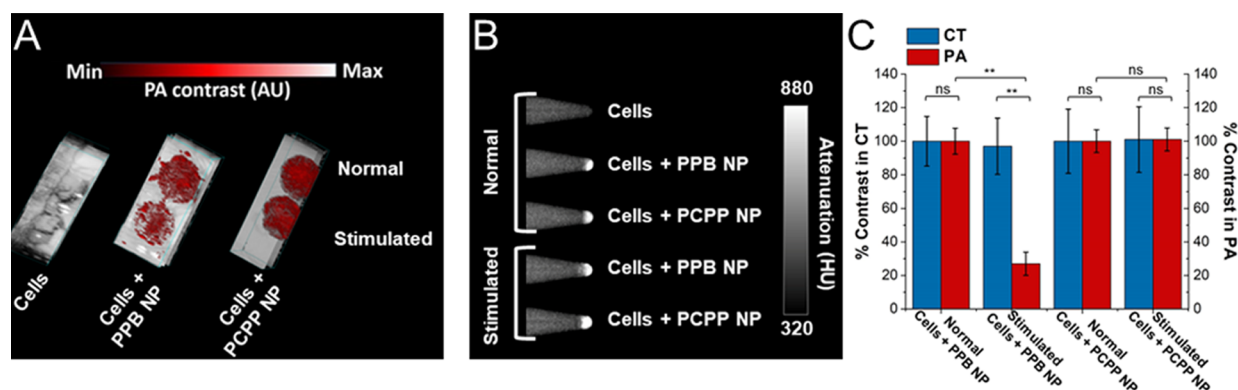


Figure 6. Influence of LPS stimulation on PA and CT contrast in macrophages incubated with PPB NP or the control PCPP NP. (A) PA images, (B) CT images, and (C) percentage of contrast enhancement in CT (blue) and PA (red) of the normal or stimulated cells incubated with PPB or PCPP NP. The symbols ** and 'ns' indicate either a statistically significant difference at $p < 0.01$ or nonstatistically significant differences, respectively. Error bars represent standard deviations after conversion to percentages.

other polymers based on a phosphazene core have been used in combination with AuNP for nanomedicine use, and notably, Hu et al. fabricated spheres of polycyclotriphosphazene and Fe_3O_4 covered in a gold nanoshell and found those nanoconstructs to have a potential as the therapeutic agent in photothermal therapy (PTT).³⁸ Particles based on polycyclotriphosphazene, whose surface was functionalized with AuNP, were shown by Wei et al. to have dual therapeutic properties in PTT and photodynamic therapy.³⁹ However, we report herein a novel ROS-responsive polymer and have fabricated the first example of ROS-responsive AuNP-polyphosphazene nanomaterials.

The ROS-triggered release of the payload content could be used to load other metal nanoparticles such as palladium NP that work cooperatively with AuNP to provide novel sensing properties.⁴⁰ Other materials could be loaded too, such as dyes that grant aggregation induced PA signal,⁴¹ or metal nanoparticles that experience an interparticle plasmon coupling effect, such as aluminium NPs that are less expensive than gold, silver that provides contrast enhancement in dual-energy mammography, and so forth.^{42,43} Accordingly, water soluble fluorescent dyes or quantum dots are also appealing for the Förster energy transfer (FRET) on–off nanoprobe by a similar mechanism of ROS-triggered disassembly to image ROS overexpression in superficial tissues.^{44–46} In addition, the ROS-responsive PPB NP could also find applications as a stimulus-responsive theranostic or delivery platform for either anticancer or antioxidant drugs by targeting the areas with high levels of ROS, therefore offering the possibility to treat inflammation and related diseases.^{47,48}

In summary, the PPB NPs loaded with sub-5 nm AuNPs have high in vitro biocompatibility and provide signal in PA due to the interparticle plasmon coupling effect of neighboring AuNP, in addition to providing strong contrast enhancement in CT allowing the nanoprobe quantification with minimal influence from their environment. Moreover, the functionalization of the polyphosphazene core of PPB with responsive arylboronate moieties grants to the PPB NP the capability to degrade under ROS exposure and release single AuNP, resulting in a significant decrease of the PA signal. Certainly, improvement in the kinetics of the ROS-triggered degradation of the free PPB by modifying the arylboronate linkage to the polyphosphazene core would be required for facilitating the translation of this technology to a clinical or preclinical setup.

However, such ROS-responsive nanogel-allowing payload release for signal switch-off in PA could be extended to other nanomaterials that are either less expensive or give access to ROS imaging with other imaging modalities. Moreover, we envision that loading small antioxidant drugs along with metal nanoparticles has the potential to image in real-time the ROS-triggered delivery of the drug and treats the source of oxidative stress overproduction using a single theranostic nanoparticle formulation.

4. CONCLUSIONS

We reported herein hybrid PPB nanoprobe that selectively disassemble when exposed to ROS and allow the ratiometric imaging of endogenous ROS by bimodal PA and CT imaging. The nanoprobe was designed to assemble excretable AuNP into polymeric nanogels composed of a biodegradable polyphosphazene backbone with a caging arylboronate moiety that degrades in the presence of ROS. These nanoprobe provide strong contrast enhancement in both CT and PA until they are exposed to ROS, which triggers the selective disassembly of the PPB NP, thus causing the release of single AuNP and PA signal reduction. The detection of ROS by comparison of PA to CT contrast in inflamed macrophages served as a proof-of concept for this on–off bimodal nanoprobe. Finally, these novel hybrid nanoprobe are biocompatible. Moreover, the tunable formulation process described herein could be adapted in the future to achieve nanotheranostics by loading ROS scavenging, antimicrobial, or anticancer drugs in the PPB NP and therefore allow a ROS-targeted therapy to treat the cause of the inflammation.

■ ASSOCIATED CONTENT

Supporting Information

The Supporting Information is available free of charge on the ACS Publications website at DOI: 10.1021/acsami.9b08386.

Polymer synthesis experimental details, physico-chemical characterization of PPB NP and PCPP NP, degradability of PPB NP by ROS species, contrast enhancement in CT and PA imaging, H_2O_2 -dose response of PPB NP, cell viability of PPB NP, and ROS and TNF- α production in macrophages (PDF)

AUTHOR INFORMATION

Corresponding Author

*E-mail: david.cormode@uphs.upenn.edu. Phone: 215-615-4656. Fax: 240-368-8096.

ORCID

Mathilde Bouché: 0000-0003-2707-1290

Andrew Tsourkas: 0000-0001-7758-1753

Ian Teasdale: 0000-0001-5953-9084

David P. Cormode: 0000-0002-8391-9500

Funding

We thank the Franco-American Commission Fulbright for fellowship support to M.B. This work was also supported by NIH (R01 HL131557, R01 CA227142, and S10 OD016310). I.T. acknowledges financial support of the Austrian Science Fund (FWF), P 27410-N28. This work was carried out in part at the Singh Center for Nanotechnology, part of the National Nanotechnology Coordinated Infrastructure Program, which is supported by the National Science Foundation grant NNCI-1542153.

Notes

The authors declare the following competing financial interest(s): D.P.C. is named as inventor on a patent application related to polyphosphazene nanoparticles and holds stock in a company, PolyAurum, that is developing gold nanoparticles for biological applications.

ACKNOWLEDGMENTS

Eric Blankemeyer and Susan Schultz from the Radiology Department at the University of Pennsylvania are kindly acknowledged for their help with the micro-CT and PA scanners, respectively.

REFERENCES

- (1) Moloney, J. N.; Cotter, T. G. ROS signalling in the Biology of Cancer. *Semin. Cell Dev. Biol.* **2018**, *80*, 50–64.
- (2) Chen, Q.; Wang, Q.; Zhu, J.; Xiao, Q.; Zhang, L. Reactive Oxygen Species: Key Regulators in Vascular Health and Diseases. *Br. J. Pharmacol.* **2018**, *175*, 1279–1292.
- (3) Morry, J.; Ngamcherdtrakul, W.; Yantasee, W. Oxidative Stress in Cancer and Fibrosis: Opportunity for Therapeutic Intervention with Antioxidant Compounds, Enzymes, and Nanoparticles. *Redox Biol.* **2017**, *11*, 240–253.
- (4) Marrocco, I.; Altieri, F.; Peluso, I. Measurement and Clinical Significance of Biomarkers of Oxidative Stress in Humans. *Oxid. Med. Cell. Longevity* **2017**, 6501046.
- (5) Nagano, T. Bioimaging Probes for Reactive Oxygen Species and Reactive Nitrogen Species. *J. Clin. Biochem. Nutr.* **2009**, *45*, 111–124.
- (6) Herman, J.; Zhang, Y.; Castranova, V.; Neal, S. L. Emerging Technologies for Optical Spectral Detection of Reactive Oxygen Species. *Anal. Bioanal. Chem.* **2018**, *410*, 6079–6095.
- (7) Wilson, K.; Homan, K.; Emelianov, S. Biomedical Photoacoustics Beyond Thermal Expansion using Triggered Nanodroplet Vaporization for Contrast-Enhanced Imaging. *Nat. Commun.* **2012**, *3*, 618.
- (8) Xia, J.; Yao, J.; Wang, L. H. V. Photoacoustic Tomography: Principles and Advances (Invited Review). *Prog. Electromagn. Res.* **2014**, *147*, 1–22.
- (9) Moore, C.; Jokerst, J. V. Strategies for Image-Guided Therapy, Surgery, and Drug Delivery using Photoacoustic Imaging. *Theranostics* **2019**, *9*, 1550–1571.
- (10) Wang, G.; Zhang, F.; Tian, R.; Zhang, L.; Fu, G.; Yang, L.; Zhu, L. Nanotubes-Embedded Indocyanine Green-Hyaluronic Acid Nanoparticles for Photoacoustic-Imaging-Guided Phototherapy. *ACS Appl. Mater. Interfaces* **2016**, *8*, S608–S617.

- (11) Chee, R. K. W.; Li, Y.; Zhang, W.; Campbell, R. E.; Zemp, R. J. In Vivo Photoacoustic Difference-Spectra Imaging of Bacteria using Photoswitchable Chromoproteins. *J. Biomed. Opt.* **2018**, *23*, 1.
- (12) Ding, H.; Cai, Y.; Gao, L.; Liang, M.; Miao, B.; Wu, H.; Liu, Y.; Xie, N.; Tang, A.; Fan, K.; Yan, X.; Nie, G. Exosome-Like Nanozyme Vesicles for H₂O₂-Responsive Catalytic Photoacoustic Imaging of Xenograft Nasopharyngeal Carcinoma. *Nano Lett.* **2019**, *19*, 203–209.
- (13) Smith, B. R.; Gambhir, S. S. Nanomaterials for in Vivo Imaging. *Chem. Rev.* **2017**, *117*, 901–986.
- (14) Yang, Z.; Song, J.; Tang, W.; Fan, W.; Dai, Y.; Shen, Z.; Lin, L.; Cheng, S.; Liu, Y.; Niu, G.; Rong, P.; Wang, W.; Chen, X. Stimuli-Responsive Nanotheranostics for Real-Time Monitoring Drug Release by Photoacoustic Imaging. *Theranostics* **2019**, *9*, 526–536.
- (15) Chen, Q.; Liang, C.; Sun, X.; Chen, J.; Yang, Z.; Zhao, H.; Feng, L.; Liu, Z. H₂O₂-Responsive Liposomal Nanoprobe for Photoacoustic Inflammation Imaging and Tumor Theranostics via in Vivo Chromogenic Assay. *PNAS* **2017**, *114*, 5343–5348.
- (16) Zhen, X.; Zhang, C.; Xie, C.; Miao, Q.; Lim, K. L.; Pu, K. Intraparticle Energy Level Alignment of Semiconducting Polymer Nanoparticles to Amplify Chemiluminescence for Ultrasensitive In Vivo Imaging of Reactive Oxygen Species. *ACS Nano* **2016**, *10*, 6400–6409.
- (17) Wang, H.; Yu, D.; Li, B.; Liu, Z.; Ren, J.; Qu, X. Ultrasensitive Magnetic Resonance Imaging of Systemic Reactive Oxygen species in vivo for Early Diagnosis of Sepsis using Activatable Nanoprobes. *Chem. Sci.* **2019**, *10*, 3770–3778.
- (18) Amendola, V.; Pilot, R.; Frascioni, M.; Maragò, O. M.; Iati, M. A. Surface Plasmon Resonance in Gold Nanoparticles: a Review. *J. Phys. Condens. Matter* **2017**, *29*, 203002.
- (19) Song, J.; Huang, P.; Duan, H.; Chen, X. Plasmonic Vesicles of Amphiphilic Nanocrystals: Optically Active Multifunctional Platform for Cancer Diagnosis and Therapy. *Acc. Chem. Res.* **2015**, *48*, 2506–2515.
- (20) He, J.; Huang, X.; Li, Y.-C.; Liu, Y.; Babu, T.; Aronova, M. A.; Wang, S.; Lu, Z.; Chen, X.; Nie, Z. Self-Assembly of Amphiphilic Plasmonic Micelle-Like Nanoparticles in Selective Solvents. *J. Am. Chem. Soc.* **2013**, *135*, 7974–7984.
- (21) Bamrungsap, S.; Chongsuwanwong, J.; Srisurat, P.; Chonirat, J.; Sangsing, N.; Wiriyaichaporn, N. Visual Colorimetric Sensing System Based on the Self-Assembly of Gold Nanorods and Graphene Oxide for Heparin Detection using a Polycationic Polymer as a Molecular Probe. *Anal. Methods* **2019**, *11*, 1387–1392.
- (22) Lin, J.; Wang, S.; Huang, P.; Wang, Z.; Chen, S.; Niu, G.; Li, W.; He, J.; Cui, D.; Lu, G.; Chen, X.; Nie, Z. Photosensitizer-Loaded Gold Vesicles with Strong Plasmonic Coupling Effect for Imaging-Guided Photothermal/Photodynamic Therapy. *ACS Nano* **2013**, *7*, 5320–5329.
- (23) Wang, Y.; Wang, L.; Yan, M.; Cai, A.; Dong, S.; Hao, J. Plasmonic Microgels of Au Nanorods: Self-Assembly and Applications in Chemophotothermo-Synergistic Cancer Therapy. *J. Colloid Interface Sci.* **2019**, *536*, 728–736.
- (24) Liu, Y.; He, J.; Yang, K.; Yi, C.; Liu, Y.; Nie, L.; Khashab, N. M.; Chen, X.; Nie, Z. Folding Up of Gold Nanoparticle Strings into Plasmonic Vesicles for Enhanced Photoacoustic Imaging. *Angew. Chem., Int. Ed.* **2015**, *54*, 15809–15812.
- (25) Kim, T.; Zhang, Q.; Li, J.; Zhang, L.; Jokerst, J. V. A Gold/Silver Hybrid Nanoparticle for Treatment and Photoacoustic Imaging of Bacterial Infection. *ACS Nano* **2018**, *12*, 5615.
- (26) Cheheltani, R.; Ezzibdeh, R. M.; Chhour, P.; Pulaparthi, K.; Kim, J.; Jurcova, M.; Hsu, J. C.; Blundell, C.; Litt, H. I.; Ferrari, V. A.; Allcock, H. A.; Sehgal, C. M.; Cormode, D. P. Tunable, Biodegradable Gold Nanoparticles as Contrast Agents for Computed Tomography and Photoacoustic Imaging. *Biomaterials* **2016**, *102*, 87–97.
- (27) Iturmendi, A.; Monkowius, U.; Teasdale, I. Oxidation Responsive Polymers with a Triggered Degradation via Arylboronate Self-Immolative Motifs on a Polyphosphazene Backbone. *ACS Macro Lett.* **2017**, *6*, 150–154.

- (28) Saha, K.; Agasti, S.S.; Kim, C.; Li, X.; Rotello, V. M. Gold Nanoparticles in Chemical and Biological Sensing. *Chem. Rev.* **2012**, *112*, 2739–2779.
- (29) Andrianov, A. K.; Marin, A.; Chen, J. Synthesis, Properties, and Biological Activity of Poly[di(sodium carboxylatoethylphenoxy)-phosphazene]. *Biomacromolecules* **2006**, *7*, 394–399.
- (30) Chhour, P.; Gallo, N.; Cheheltani, R.; Williams, D.; Al-Zaki, A.; Paik, T.; Nichol, J. L.; Tian, Z.; Naha, P. C.; Witschey, W. R.; Allcock, H. R.; Murray, C. B.; Tsourkas, A.; Cormode, D. P. Nanodisco Balls: Control Over Surface versus Core Loading of Diagnostically Active Nanocrystals into Polymer Nanoparticles. *ACS Nano* **2014**, *8*, 9143–9153.
- (31) Allcock, H. R.; Morozowich, N. L. Bioerodible Polyphosphazenes and Their Medical Potential. *Polym. Chem.* **2012**, *3*, 578–590.
- (32) Hajfathalian, M.; Bouché, M.; Cormode, D. P. Polyphosphazene-Based Nanoparticles as Contrast Agents for Medical Imaging. Chapter in *Polyphosphazenes in Biomedicine, Engineering, and Pioneering Synthesis*; Oxford University Press, 2018; 77–100.
- (33) Pu, K.; Shuhendler, A. J.; Jokerst, J. V.; Mei, J.; Gambhir, S. S.; Bao, Z.; Rao, J. Semiconducting Polymer Nanoparticles as Photoacoustic Molecular Imaging Probes in Living Mice. *Nat. Nanotechnol.* **2014**, *9*, 233–239.
- (34) Peterson, G. I.; Larsen, M. B.; Boydston, A. J. Controlled Depolymerization: Stimuli-Responsive Self-Immulative Polymers. *Macromolecules* **2012**, *45*, 7317–7328.
- (35) Li, M.; Li, S.; Chen, H.; Hu, R.; Liu, L.; Lv, F.; Wang, S. Preparation of Conjugated Polymer Grafted with H₂O₂-Sensitive Prodrug for Cell Imaging and Tumor Cell Killing. *ACS Appl. Mater. Interfaces* **2016**, *8*, 42–46.
- (36) de Gracia Lux, C.; Joshi-Barr, S.; Nguyen, T.; Mahmoud, E.; Schopf, E.; Fomina, N.; Almutairi, A. Biocompatible Polymeric Nanoparticles Degrade and Release Cargo in Response to Biologically Relevant Levels of Hydrogen Peroxide. *J. Am. Chem. Soc.* **2012**, *134*, 15758–15764.
- (37) Broaders, K. E.; Grandhe, S.; Fréchet, J. M. J. A Biocompatible Oxidation-Triggered Carrier Polymer with Potential in Therapeutics. *J. Am. Chem. Soc.* **2011**, *133*, 756–758.
- (38) Hu, Y.; Meng, L.; Niu, L.; Lu, Q. Facile Synthesis of Superparamagnetic Fe₃O₄@polyphosphazene@Au Shells for Magnetic Resonance Imaging and Photothermal Therapy. *ACS Appl. Mater. Interfaces* **2013**, *5*, 4586–4591.
- (39) Wei, X.; Chen, H.; Tham, H. P.; Zhang, N.; Xing, P.; Zhang, G.; Zhao, Y. Combined Photodynamic and Photothermal Therapy Using CrossLinked Polyphosphazene Nanospheres Decorated with Gold Nanoparticles. *ACS Appl. Nano Mater.* **2018**, *1*, 3663–3672.
- (40) Lerch, S.; Reinhard, B. M. Effect of Interstitial Palladium on Plasmon-Driven Charge Transfer in Nanoparticle Dimers. *Nat. Commun.* **2018**, *9*, 1608.
- (41) An, F. F.; Deng, Z. J.; Ye, J.; Zhang, J. F.; Yang, Y. L.; Li, C. H.; Zheng, C. J.; Zhang, X. H. Aggregation-Induced Near-Infrared Absorption of Squaraine Dye in an Albumin Nanocomplex for Photoacoustic Tomography in Vivo. *ACS Appl. Mater. Interfaces* **2014**, *6*, 17985–17992.
- (42) Trautmann, S.; Richard-Lacroix, M.; Dathe, A.; Schneidewind, H.; Dellith, J.; Fritzsche, W.; Deckert, V. Plasmon Response Evaluation Based on Image-Derived Arbitrary Nanostructures. *Nanoscale* **2018**, *10*, 9830–9839.
- (43) Guerrini, L.; Graham, D. Molecularly-Mediated Assemblies of Plasmonic Nanoparticles for Surface-Enhanced Raman Spectroscopy Applications. *Chem. Soc. Rev.* **2012**, *41*, 7085–7107.
- (44) Hildebrand, N.; Spillmann, C. M.; Algar, W. R.; Pons, T.; Stewart, M. H.; Oh, E.; Susumu, K.; Díaz, S. A.; Delehanty, J. B.; Medintz, I. L. Energy Transfer with Semiconductor Quantum Dot Bioconjugates: a Versatile Platform for Biosensing, Energy Harvesting, and Other Developing Applications. *Chem. Rev.* **2017**, *117*, 536–711.
- (45) Ma, T.; Zeng, J.; Liu, C.; Zhang, P.; Jing, L.; Shangguan, D.; Gao, M. Dual-Ratiometric Target-Triggered Fluorescent Probe for Simultaneous Quantitative Visualization of Tumor Microenvironment Protease Activity and pH in Vivo. *J. Am. Chem. Soc.* **2018**, *140*, 211–218.
- (46) Chen, Z.; Liu, Z.; Li, Z.; Ju, E.; Gao, N.; Zhou, L.; Ren, J.; Qu, X. Upconversion nanoprobe for efficiently in vitro imaging reactive oxygen species and in vivo diagnosing rheumatoid arthritis. *Biomaterials* **2015**, *39*, 15–22.
- (47) Sun, Q.; He, F.; Sun, C.; Wang, X.; Li, C.; Xu, J.; Yang, D.; Bi, H.; Gai, S.; Yang, P. Honeycomb-Satellite Structured pH/H₂O₂-Responsive Degradable Nanoplatfor for Efficient Photodynamic Therapy and Multimodal Imaging. *ACS Appl. Mater. Interfaces* **2018**, *10*, 33901–33912.
- (48) Yang, B.; Chen, Y.; Shi, J. Reactive Oxygen Species (ROS)-Based Nanomedicine. *Chem. Rev.* **2019**, *119*, 4881–4985.